A Novel Method for Vibration Analysis of an Infinite AT-Cut Quartz Resonator with Irregularly-Shaped Electrodes

Chen Yang[1], Peng Li[1, 2], Xueli Zhao[1], Bin Wang[1, 2], Iren Kuznetsova[3], Dianzi Liu[4], Zhenghua Qian[1, 2, *], Vladimir Kolesov[3]

1 State Key Laboratory of Mechanics and Control of Mechanical Structures, College of Aerospace Engineering, Nanjing University of Aeronautics and Astronautics, Nanjing 210016, China

2 Nanjing University of Aeronautics and Astronautics Shenzhen Research Institute, Shenzhen, 518057, China

3 Kotel'nikov Institute of Radio Engineering and Electronics of RAS, Moscow 125009, Russia

4 School of Engineering, University of East Anglia, Norwich NR4 7TJ, U.K.

*Correspondence author, E-mail: qianzh@nuaa.edu.cn

Abstract

A novel method for solving thickness shear vibration in an AT-cut quartz plate with partial irregularly-shaped electrodes is proposed. Firstly, two-dimensional scalar differential equations derived by Tiersten and Smythe are adopted and transformed into the polar coordinate system. Secondly, displacement patterns for the electroded and unelectroded regions are assumed as a series of converging and outgoing cylindrical wave in the form of Bessel functions, where Sommerfeld radiation conditions at infinity can be satisfied automatically. Finally, circumferential functions at interface are decomposed into Fourier series in order to deal with continuous conditions. It should be stressed that the general formulation proposed in this paper has a higher calculation accuracy, which can satisfy continuous conditions in an integrated manner over the whole interface or boundary. Resonant frequencies and mode shapes of different electrode shapes including circular, equilateral triangle, rectangular, elliptical, and pentagonal electrodes are numerically calculated and compared with FEM simulations, which efficiently validate high precision and wide applicability of this method. Utilizing this method, the influence of irregularly-shaped electrodes on the working performance of the AT-cut quartz resonator is investigated systematically. The qualitative analysis and quantitative results obtained in this paper

can provide the theoretical guidance for the design, measurement and manufacturing optimization of quartz crystal resonators.

1. Introduction

Due to the high sensitivity and stability, piezoelectric crystals have been widely used in electronic devices, such as acoustic wave resonators for time-keeping, generators in telecommunications for frequency control, harvesters for energy transformation and collection, mass and liquid sensors for performance estimation, and so forth. Quartz crystal is the most favorable piezoelectric material for manufacturing resonators because of its superior properties, including the outstanding piezoelectric abilities, high quality factors, good temperature stabilities and long service life. Therefore, the working performance of quartz crystal resonators (QCRs) has been extensively concerned in the academic research and engineering applications, and the research priorities mainly focus on the new-type structural design, frequency stability, sensitivity on some external stimulus (temperature, humidity, and electromagnetic field), the quality factor and potential applications in the micro-nano scale [1, 2].

Generally speaking, resonators and acoustic wave devices made of quartz are very thin, with the thickness is much smaller than the other size in length and width directions. Correspondingly, some working modes exist in plate-type structures, such as thickness extensional (TE) modes, thickness-shear (TSh) modes [3], thickness-twist (TT) modes, and so on. Mostly, these modes are coupled together because of the anisotropy. However, some pure working modes can be generated successfully in some frequency regions via properly designing the crystal size and optimizing the electrodes attached on the plate surface. For instance, TSh modes that have slow in-plane variations and sometimes are termed as transversely varying modes [4], can be decoupled from others and viewed as the main operating modes of QCRs.

For resonators based on TSh vibration, the electrode partially distributed on the plate surface plays an important role. Modes are generated via the electric fields imposed on the electrodes. Additionally, the energy trapping phenomenon can also be realized via partial electrodes [5]. After

properly choosing the working frequency, the TSh vibration energy can be trapped in the region with electrodes and decays rapidly when departing from electrodes. It is crucial for the mounting and installing of wave devices. Based on the energy trapping phenomenon, the terminal pins or holders can be fixed far away from the electrode region, and the central TSh vibration hardly affect them. For achieving excellent trapped modes [6], more and more contributions are concerning the electrode design and optimization.

Most of electrodes in QCRs are rectangular. In recent years, circular [7], polygonal [8], elliptical [9, 10] or other electrodes with different profiles [11] are introduced into the resonators, which also exhibit good performances at trapping vibration energy. Not limited by this, the electrodes with complex profile can efficiently suppress spurious modes unwanted. For example, Wu et al. [12] analyzed the thickness-shear vibrations of an AT-cut quartz piezoelectric crystal plate with elliptical ring electrodes to realize the desired trapped mode with suitable center convexity for wave sensing. He et al. [13] studied the TSh vibration of a QCR with rectangular electrodes. However, owing to the anisotropy of piezoelectric materials and the electro-mechanical coupling effect, finding a theoretical solution of QCRs with irregular electrodes is very difficult [14]. Indeed, the finite element method (FEM) is usually utilized to capture the vibration characteristics [15-17]. In principle, the TSh vibration of quartz crystal plats with any electrodes can be solved via FEM. However, there are still many limitations and disadvantages, since the FEM consumes a large amount of time for computation, especially for the increased meshes and matrix scale when analyzing high-order modes. During FEM simulations, a large number of coupled modes and spurious modes exist around the working frequency, which are not convenient for data processing. Without theoretical analysis, some physical mechanisms are not easy to reveal [18-21]. Therefore, it is necessary to find a general theoretical solution to depict the resonator vibration properties, which is suitable for arbitrary electrodes with any profiles. This is the origin, as well as the highlight of the present contribution.

In order to achieve this aim, systematic two-dimensional (2-D) scalar differential equations for pure TSh modes derived by Tiersten and his colleagues [22-25] are adopted, which have been proved effectively and accurately in analyzing the fundamental and overtone frequencies in an AT-cut resonator. The contour of electrodes bonded on the plate surfaces is arbitrary, and defined

by a mathematical function during the theoretical analysis. After coordinate transformation, the displacement component in different regions is expressed in the form of Bessel functions, and the Fourier series expansion is adopted for satisfying the continuous boundary in Section 2. Different from the perturbation method developed by Tiersten [23] and the collocation method conducted by Wang et al. [7] and Zhu et al. [26], the theoretical solutions proposed in this paper is more rigorous with more accuracy, which can strictly satisfy the dynamic governing equations and the corresponding boundary conditions. In Section 3, the convergence of this series is illustrated, and the theoretical solution is validated by comparing the resonant frequencies and mode shapes with those from the COMSOL Multiphysics software. Furthermore, the resonator performance is quantitatively demonstrated when pentagonal electrodes are considered. Finally, some conclusions are drawn in Section 4. It is anticipated that this method proposed in this paper is still available for other electronic devices with the similar configurations, *e.g.*, thin film bulk acoustic resonators (FBARs), quartz crystal microbalances (QCMs), and so forth.

2. Fundamental theory of free vibration analysis

2.1. Governing equations

For the theoretical analysis, an infinite AT-cut quartz plate with a pair of symmetrical partial electrodes placed on the top and bottom surfaces is considered, such as **Figure 2.1**. The thickness values of the plate and the electrodes are respectively represented by $2h$ and h_e. In this paper, the electrode is irregular, *e.g.*, circular, elliptical, rectangular, triangle and so forth. For convenience, a geometric function $R_0(x_1, x_3)$ is adopted to mathematically describe the electrode profile during analysis, *i.e.*, the electrode/unelectroded interface in the x_1-x_3 plane. Therefore, different expressions related to R_0 stand for different electrodes. For example, if $R_0(x_1, x_3)=x_1^2+x_3^2=C^2$ with a constant value C, the electrode profile is circular. A smooth function of R_0 with respect to circumferential position θ denotes elliptical electrodes. The emphasis of this contribution is establishing a theoretical model, which can exactly depict the influence of electrodes with arbitrary shape on the TSh waves propagation in the AT-cut quartz plate.
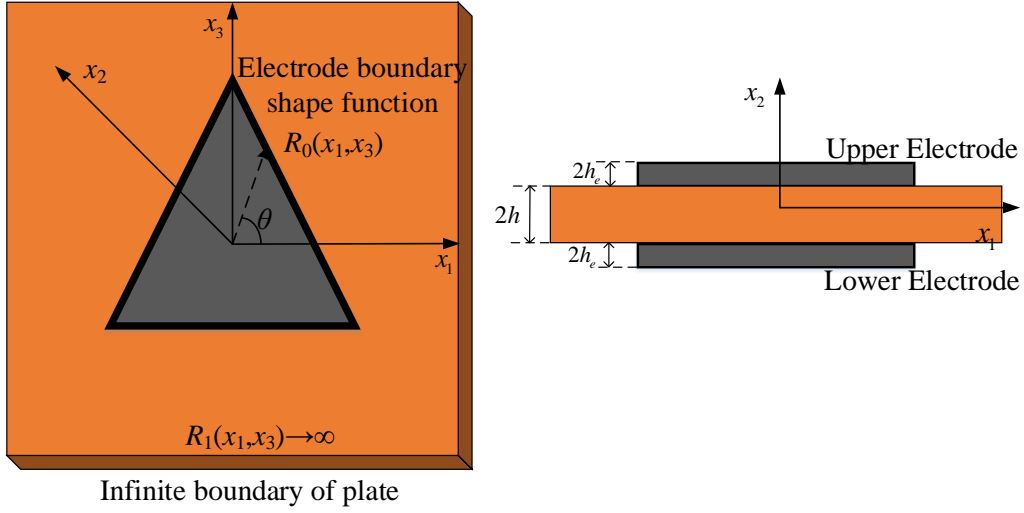
Figure 2.1 An AT-cut quartz plate with partial electrodes, in which the left schematic diagram is the top view and another is the front view.

After simplifying assumptions of small piezoelectric coupling and ignoring small elastic constant, the dynamic equations that governing coupled TSh vibration in quartz plates can be derived as

$$
\begin{aligned}
&c_{11}u_{1,11} + (c_{12} + c_{66})u_{2,12} + c_{66}u_{1,22} + c_{55}u_{1,33} + e_{26}\varphi_{,22} = \rho\ddot{u}_1, \\
&(c_{12} + c_{66})u_{1,12} + c_{66}u_{2,11} + c_{22}u_{2,22} = \rho\ddot{u}_2, \\
&e_{26}u_{1,22} - \varepsilon_{22}\varphi_{,22} = 0.
\end{aligned}
\tag{1}
$$

Here, u_1 and u_2 are displacement components, and φ is the electrical potential function. c_{11}, c_{12}, c_{22}, c_{55} and c_{66} are elastic constants. e_{26} and ε_{22} respectively denote the piezoelectric and dielectric constants. Correspondingly, the constitutive equations related to stress components T_{21}, T_{22}, T_{11}, and T_{13} and electric displacement component D_2 are

$$
\begin{aligned}
&T_{21} = c_{66}(u_{1,2} + u_{2,1}) + e_{26}\varphi_{,2}, \quad T_{22} = c_{12}u_{1,1} + c_{22}u_{2,2}, \\
&T_{11} = c_{11}u_{1,1} + c_{12}u_{2,2}, \quad T_{13} = c_{55}u_{1,3} + e_{25}\varphi_{,2}, \\
&D_2 = e_{26}u_{1,2} - \varepsilon_{22}\varphi_{,2}.
\end{aligned}
\tag{2}
$$

The well-known Tiersten's 2-D scalar differential equations that control the TSh vibration with only one dominate displacement component $u_1(x_1, x_2, x_3, t)$ are adopted in this paper. For **Figure 2.1** concerned, the displacement can be written in the superposition form of all anti-symmetric modes and symmetric modes along the x_2 direction, *i.e.* [22, 24]

$$
u_1(x_1, x_2, x_3, t) = \sum_{n=1,3,5\dots}^{+\infty} \square^n(x_1, x_3)\sin(\frac{n\pi x_2}{2h})\exp(i\omega t) = \sum_{n=1,3,5\dots}^{+\infty} \square^n(x_1, x_3)W_n^h(x_2)\exp(i\omega t)
\tag{3}
$$

for the electroded region, and

$$u_1(x_1, x_2, x_3, t) = \sum_{n=0,2,4\ldots}^{+\infty} \square^n(x_1, x_3)\cos(\frac{n\pi x_2}{2h})\exp(i\omega t) = \sum_{n=0,2,4\ldots}^{+\infty} \square^n(x_1, x_3)V_n^h(x_2)\exp(i\omega t) \quad (4)$$

for the unelectroded region. Here, $n=1$ represents the fundamental operating mode, while other values of n such as $n=1,3,5,\cdots$ and $n=0,2,4,\cdots$ are high-order overtones. For the free vibration analysis of quartz resonators with a circular frequency ω, all variations have the same harmonic time factor $\exp(i\omega t)$, which will be neglected below for simplification. $\square^n(x_1, x_3)$ and $\square^n(x_1, x_3)$ represent the nth order TSh displacement with in-plane variation, which are respectively governed by

$$\begin{cases} M_n \dfrac{\partial^2 \square^n(x_1, x_3)}{\partial x_1^2} + c_{55}\dfrac{\partial^2 \square^n(x_1, x_3)}{\partial x_3^2} + \rho(\omega^2 - \bar{\omega}_\infty^2)\square^n(x_1, x_3) = 0, \\ M_n \dfrac{\partial^2 \square^n(x_1, x_3)}{\partial x_1^2} + c_{55}\dfrac{\partial^2 \square^n(x_1, x_3)}{\partial x_3^2} + \rho(\omega^2 - \omega_\infty^2)\square^n(x_1, x_3) = 0 \end{cases} \quad (5)$$

for the electroded and unelectroded regions [22] respectively. Correspondingly,

$$M_n = c_{11} + (c_{12} + c_{66})r' + \frac{4(r'\bar{c}_{66} - c_{66})(r'c_{22} + c_{12})}{c_{22}n\pi\kappa}\cot\frac{\kappa n\pi}{2}, \quad (6)$$

$$\bar{c}_{66} = c_{66} + \frac{e_{26}^2}{\varepsilon_{22}}, \quad \kappa = \left(\frac{\bar{c}_{66}}{c_{22}}\right)^{1/2}, \quad r' = \frac{c_{12} + c_{66}}{\bar{c}_{66} - c_{22}}. \quad (7)$$

The intrinsic fundamental frequencies $\bar{\omega}_\infty$ or ω_∞ of an infinite electroded or unelectroded plate is [24]

$$\bar{\omega}_\infty = \frac{n\pi}{2h}\sqrt{\frac{\hat{c}_{66}}{\rho}}, \quad \omega_\infty = \frac{n\pi}{2h}\sqrt{\frac{\bar{c}_{66}}{\rho}}, \quad (8)$$

with

$$\hat{c}_{66} = \bar{c}_{66}(1 - \frac{8\bar{k}_{26}^2}{n^2\pi^2} - 2R), \quad \bar{k}_{26}^2 = \frac{e_{26}^2}{\bar{c}_{66}\varepsilon_{22}}, \quad R = \frac{2\rho_e h_e}{\rho h}. \quad (9)$$

$\bar{k}_{26}^2$ is the electromechanical coupling factor, which can depict the transformation ability between the electrical energy and the mechanical deformation. R stands for the mass ratio with ρ and ρ_e respectively being the mass density of the quartz plate and electrodes. After introducing a coordinate transformation in the x_1-x_3 plane for both the electroded and unelectroded regions

$$y_1 = x_1 \text{ and } y_3 = \mu x_3 \quad (10)$$

with $\mu = \sqrt{M_n / c_{55}}$, **Eq. (5)** can be rewritten as

$$
\begin{cases}
M_n[\dfrac{\partial^2 \square^n(y_1,y_3)}{\partial y_1^2} + \dfrac{\partial^2 \square^n(y_1,y_3)}{\partial y_3^2}] + \rho(\omega^2 - \bar{\omega}_\infty^2)\square^n(y_1,y_3) = 0, \\[4mm]
M_n[\dfrac{\partial^2 \square^n(y_1,y_3)}{\partial y_1^2} + \dfrac{\partial^2 \square^n(y_1,y_3)}{\partial y_3^2}] + \rho(\omega^2 - \omega_\infty^2)\square^n(y_1,y_3) = 0.
\end{cases}
\tag{11}
$$

Meanwhile, the boundary function $R_0(x_1, x_3)$ of the electrode is also transformed into $R_0(y_1, y_3)$ in the new coordinate system. For instance, an annular boundary $x_1^2 + x_3^2 = C^2$ can be redefined as an elliptical boundary $y_1^2 / C^2 + y_3^2 / (\mu C)^2 = 1$ after the coordinate transformation. Therefore, **Eq. (11)** can be expressed in the following more compact form:

$$
\begin{aligned}
&\frac{\partial^2 \square^n(r,\theta)}{\partial r^2} + \frac{1}{r}\frac{\partial \square^n(r,\theta)}{\partial r} + \frac{1}{r^2}\frac{\partial^2 \square^n(r,\theta)}{\partial \theta^2} + \bar{\alpha}^2 \square^n(r,\theta) = 0, \text{ when } r \le R_0(\theta), \\[3mm]
&\frac{\partial^2 \square^n(r,\theta)}{\partial r^2} + \frac{1}{r}\frac{\partial \square^n(r,\theta)}{\partial r} + \frac{1}{r^2}\frac{\partial^2 \square^n(r,\theta)}{\partial \theta^2} - \hat{\alpha}^2 \square^n(r,\theta) = 0, \text{ when } r \ge R_0(\theta),
\end{aligned}
\tag{12}
$$

with

$$
\bar{\alpha}^2 = \rho(\frac{\omega^2}{\omega_\infty^2} - \frac{\bar{\omega}_\infty^2}{\omega_\infty^2}), \quad \hat{\alpha}^2 = \rho(\frac{\omega_\infty^2}{\omega_\infty^2} - \frac{\omega^2}{\omega_\infty^2}).
\tag{13}
$$

In this paper, the energy trapping phenomenon is considered, *i.e.*, the resonant frequency ω locates in the region $\bar{\omega}_\infty < \omega < \omega_\infty$, and thus both $\bar{\alpha}^2$ and $\hat{\alpha}^2$ are positive. In the following section, the solutions of **Eq. (12)** will be derived for the TSh vibration in the electrode and unelectroded regions.

2.2. Displacement fields in the new coordinate

Then we model this scattered phenomenon using three-dimensional scattering field theory. The solution of the Helmholtz equation **(12)** can be written as a combination of a radial function of r and an angular function of θ. Hence, after the variable separation, a general solution of the scalar potential functions $\square^n(r,\theta)$ and $\square^n(r,\theta)$ in **Eq. (12)** can be assumed as

$$
\begin{cases}
\square^n(r,\theta) = \displaystyle\sum_{m=0}^{\infty} \phi_m(\bar{\alpha}r)e^{im\theta}, \text{ when } r \le R_0(\theta), \\[4mm]
\square^n(r,\theta) = \displaystyle\sum_{m=0}^{\infty} \varphi_m(\hat{\alpha}r)e^{im\theta}, \text{ when } r \ge R_0(\theta).
\end{cases}
\tag{14}
$$

Here, the θ-dependency of the fields can also be assumed as $\cos(m\theta)$ for symmetric modes and

$\sin(m\theta)$ for anti-symmetric modes where $m = 0, 1, 2, \cdots$. Substituting **Eq. (14)** into **Eq. (12)**, two partial differential equations governing the scalar potential functions $\phi_m(\bar{\alpha}r)$ and $\varphi_m(\hat{\alpha}r)$ can be obtained as

$$
\begin{cases}
\dfrac{\partial^2 \phi_m(\bar{\alpha}r)}{\partial r^2} + \dfrac{1}{r}\dfrac{\partial \phi_m(\bar{\alpha}r)}{\partial r} + (\bar{\alpha}^2 - \dfrac{m^2}{r^2})\phi_m(\bar{\alpha}r) = 0, \text{ when } r \leq R_0(\theta), \\
\dfrac{\partial^2 \varphi_m(\hat{\alpha}r)}{\partial r^2} + \dfrac{1}{r}\dfrac{\partial \varphi_m(\hat{\alpha}r)}{\partial r} - (\hat{\alpha}^2 + \dfrac{m^2}{r^2})\varphi_m(\hat{\alpha}r) = 0, \text{ when } r \geq R_0(\theta).
\end{cases}
\tag{15}
$$

It should be noted that the two equations in **Eq. (15)** are the Bessel function and modified Bessel function equations of order *m*, respectively. Hence, the general solutions can be described as:

$$
\begin{cases}
\Box^n(r,\theta) = \displaystyle\sum_{m=-\infty}^{+\infty} A_m J_m(\bar{\alpha}r)e^{im\theta} + C_m Y_m(\bar{\alpha}r)e^{im\theta}, \text{ when } r \leq R_0(r,\theta), \\
\Box^n(r,\theta) = \displaystyle\sum_{m=-\infty}^{+\infty} B_m K_m(\hat{\alpha}r)e^{im\theta} + D_m I_m(\hat{\alpha}r)e^{im\theta}, \text{ when } r \geq R_0(r,\theta).
\end{cases}
\tag{16}
$$

Here, A_m, B_m, C_m and D_m are undetermined constants that will be determined by boundary conditions. J_m and Y_m are the *m*th-order Bessel function of the first and second kind, respectively. Correspondingly, I_m and K_m represent the *m*th-order modified Bessel function of the first and second kind, respectively.

2.3. Boundary and continuity conditions

For the TSh vibration, the displacement is finite when *r* approaches to zero, and it will be infinity if $r \to \infty$. Then, the terms containing $Y_m(\bar{\alpha}r)$ in **Eq. (16)** with singularity at $r = 0$, and those terms containing $I_m(\hat{\alpha}r)$ which diverge at $r \to \infty$ should be dropped. Therefore, **Eq. (16)** reduces as

$$
\begin{cases}
\Box^n(r,\theta) = \displaystyle\sum_{m=-\infty}^{+\infty} A_m J_m(\bar{\alpha}r)e^{im\theta}, \text{ when } r \leq R_0(\theta), \\
\Box^n(r,\theta) = \displaystyle\sum_{m=-\infty}^{+\infty} B_m K_m(\hat{\alpha}r)e^{im\theta}, \text{ when } r \geq R_0(\theta).
\end{cases}
\tag{17}
$$

By virtue of the theoretical solutions above, the continuity of displacement and stress components at the electrode/unelectroded interface [27, 28] requires

$$
\left.\frac{\partial \Box^n(r,\theta)}{\partial n}\right|_{r=R_0(\theta)} = \left.\frac{\partial \Box^n(r,\theta)}{\partial n}\right|_{r=R_0(\theta)}, \quad \left.\Box^n(r,\theta)\right|_{r=R_0(\theta)} = \left.\Box^n(r,\theta)\right|_{r=R_0(\theta)}.
\tag{18}
$$

In order to satisfy the boundary conditions above, we substitute **Eq. (17)** into the boundary conditions above, and obtain

$$\sum_{m=-\infty}^{+\infty} \phi_m(\bar{\alpha} r)e^{im\theta} = \sum_{m=-\infty}^{+\infty} \varphi_m(\bar{\alpha} r)e^{im\theta},$$

$$\sum_{m=0}^{\infty} \frac{\partial \phi_m(\bar{\alpha} r)}{\partial r} n_r e^{im\theta} + \sum_{m=0}^{\infty} \frac{im\phi_m(\bar{\alpha} r)}{r} n_\theta e^{im\theta} = \sum_{m=0}^{\infty} \frac{\partial \varphi_m(\bar{\alpha} r)}{\partial r} n_r e^{im\theta} + \sum_{m=0}^{\infty} \frac{im\varphi_m(\bar{\alpha} r)}{r} n_\theta e^{im\theta}. \tag{19}$$

2.4. Expansion in Fourier series

Taking the special case of elliptical electrodes for instance, it is assumed that the ratio of the major axis to the minor axis is μ in the x_1-x_3 plane. After the coordinate transformation, the boundary becomes a circle in the new y_1-y_3 plane, *i.e.*, $y_1^2 + y_3^2 = C^2$, and then $n_r(\theta) = 1$ and $n_\theta(\theta) = 0$. Under this condition, **Eq.** Error! Reference source not found. is simplified as

$$\sum_{m=-\infty}^{+\infty} A_m J_m(\bar{\alpha} r)e^{im\theta} \bigg|_{r=C} = \sum_{m=-\infty}^{+\infty} B_m K_m(\hat{\alpha} r)e^{im\theta} \bigg|_{r=C},$$

$$\sum_{m=-\infty}^{+\infty} A_m J'_m(\bar{\alpha} r)\bar{\alpha} e^{im\theta} \bigg|_{r=C} = \sum_{m=-\infty}^{+\infty} B_m K'_m(\hat{\alpha} r)\hat{\alpha} e^{im\theta} \bigg|_{r=C}. \tag{20}$$

After adopting the orthogonality of $e^{im\theta}$ to eliminate the angular coordinate θ, we get

$$\begin{bmatrix} J_m(\bar{\alpha} C) & -K_m(\hat{\alpha} C) \\ J'_m(\bar{\alpha} C)\bar{\alpha} & -K'_m(\hat{\alpha} C)\hat{\alpha} \end{bmatrix} \begin{bmatrix} A_m \\ B_m \end{bmatrix} = 0. \tag{21}$$

For nontrivial solutions, the determinant of the coefficient matrix about A_m and B_m for every m should be zero, from which the frequency equation of TSh vibration can be achieved.

However, **Eq. (21)** is only suitable for elliptical electrodes. For electrodes with arbitrary profiles, theoretical solutions are not straightforward anymore. Considering the periodicity of r, $n_r(\theta)$ and $n_\theta(\theta)$, we may obtain

$$n(\theta) = \begin{pmatrix} n_r(\theta) \\ n_\theta(\theta) \\ 0 \end{pmatrix} = \frac{1}{\sqrt{R_0(\theta)^2 + R'_0(\theta)^2}} \begin{pmatrix} R_0(\theta) \\ -R'_0(\theta) \\ 0 \end{pmatrix}, \tag{22}$$

in which $R(\theta)$ and $R'(\theta)$ respectively denote ××× and ×××. For solving this problem, the θ-dependent function in the form of Fourier series is developed in this paper, so that **Eq.**Error! Reference source not found. can be expressed as

$$\sum_{m=-\infty}^{+\infty}\sum_{q=-\infty}^{+\infty}A_m\frac{1}{2\pi}\int_{-\pi}^{\pi}J_m\left(\bar{\alpha}r(\theta)\right)e^{im\theta}e^{-iq\theta}d\theta e^{iq\theta}=\sum_{m=-\infty}^{+\infty}\sum_{q=-\infty}^{+\infty}B_m\frac{1}{2\pi}\int_{-\pi}^{\pi}K_m\left(\hat{\alpha}r(\theta)\right)e^{im\theta}e^{-iq\theta}d\theta e^{iq\theta},$$

$$\sum_{m=-\infty}^{+\infty}\sum_{q=-\infty}^{+\infty}A_m\aleph_{q,m}(\omega)e^{iq\theta}=\sum_{m=-\infty}^{+\infty}\sum_{q=-\infty}^{+\infty}B_m\Re_{q,m}(\omega)e^{iq\theta},$$

(23)

with

$$\aleph_{q,m}(\omega)=\frac{1}{2\pi}\int_{-\pi}^{\pi}\left[J_m'\left(\bar{\alpha}r(\theta)\right)\bar{\alpha}n_r(\theta)+\frac{im}{r}J_m\left(\bar{\alpha}r(\theta)\right)n_\theta(\theta)\right]e^{im\theta}e^{-iq\theta}d\theta,$$

$$\Re_{q,m}(\omega)=\frac{1}{2\pi}\int_{-\pi}^{\pi}\left[K_m'\left(\hat{\alpha}r(\theta)\right)\hat{\alpha}n_r(\theta)+\frac{im}{r}K_m\left(\hat{\alpha}r(\theta)\right)n_\theta(\theta)\right]e^{im\theta}e^{-iq\theta}d\theta.$$

(24)

Here q denotes qth term of the Fourier series. The orthogonality of the $e^{iq\theta}$ provides us convenience for eliminating the angular coordinate θ, and then **Eq. Error! Reference source not found.** can be expanded as

$$\begin{pmatrix}\wp & \Im\\ \Re & \aleph\end{pmatrix}\begin{pmatrix}A\\ B\end{pmatrix}=0,$$

(25)

in which

$$\left[\wp\right]_{p,m}=\frac{1}{2\pi}\int_{-\pi}^{\pi}J_m\left(\bar{\alpha}r(\theta)\right)e^{im\theta}e^{-iq\theta}d\theta\quad\left[\Re\right]_{p,m}=\Re_{q,m}(\omega),$$

$$\left[\Im\right]_{p,m}=\frac{1}{2\pi}\int_{-\pi}^{\pi}K_m\left(\hat{\alpha}r(\theta)\right)e^{im\theta}e^{-iq\theta}d\theta\quad\left[\aleph\right]_{p,m}=\aleph_{q,m}(\omega),$$

(26)

with the series truncation represented by *M*. Similarly with the discussion above, the frequency equation of TSh vibration can be achieved via letting the determinant of the coefficient matrix in **Eq. (25)** equaling to zero.

Up to now, the TSh vibration of an infinite AT-cut quartz plate with a pair of symmetrical arbitrary electrodes has been theoretically analyzed, and the frequency equation is derived which satisfies the governing equations and continuous conditions at the electrode/unelectroded interface. Generally speaking, the frequency equation is implicit, from which the resonant frequency can't be obtained directly. In this paper, the modulus convergence method is adopted to numerically calculate the resonant frequency from the univariate transcendental equation [31]. After discretizing the frequency region concerned into several discrete points, the minimal modulus of the equations is determined by comparing the determinant moduli at different discrete nodes. Then, the final solutions are distinguished from these points of minimum modulus according to the convergence criterion.

3. Effect of irregularly-shaped electrodes

3.1. Numerical validation

Before numerical simulations, it is necessary to examine the series convergence and validate the theoretical model established in the previous section. Without loss of generality, the resonant frequencies and mode shapes of an infinite circular AT-cut quartz resonator with different electrodes that are calculated via **Eq.** (25) will be compared with those from FEM simulations. A typical quart crystal plate with the thickness $2h = 1$mm is chosen as an example with its material parameters from Ref. [29], and the mass ratio is taken as $R = 0.05$. The fundamental operating mode with $n = 1$ that is usually encountered during applications is considered in this paper. For convergence, Tables 3.1 and 3.2 illustrate the resonant frequencies after using different M values for circular and equilateral triangle electrodes, respectively. The interface of circular electrodes can be mathematically depicted using a continuous differentiable function, and then a small M value, *e.g.*, 12, can ensure the calculation accuracy. However, for equilateral triangle electrodes, the function for mathematically depicting the electrode interface is non-differentiable, which needs more terms for obtaining a convergent result. Despite of those, both of tables indicate that the series possess a good convergence.

Table 3.1   Resonant frequencies calculated using different truncated series when circular electrodes are attached.

Truncated series	ω (10^8 rad/s)		
	$R_0 = 0.4$ mm	$R_0 = 0.6$ mm	$R_0 = 0.8$ mm
$M = 4$	1.01443020573	1.00264519552	0.99690995317
$M = 6$	1.01443041295	1.00264533555	0.99691004851
$M = 8$	1.01443042434	1.00264534285	0.99691005346
$M = 10$	1.01443042494	1.00264534321	0.99691005370
$M = 12$	1.01443042497	1.00264534322	0.99691005370
$M = 14$	1.01443042497	1.00264534322	0.99691005370
$M = 16$	1.01443042497	1.00264534322	0.99691005370

Table 3.2   Resonant frequencies calculated using different truncated series when equilateral triangle electrodes are attached.

Truncated series	ω (10^8 rad/s)		
	Scale up to 1	Scale up to 1.1	Scale up to 1.2
$M = 30$	0.99596753497	0.99464819186	0.99358914559
$M = 33$	0.99596913917	0.99464958199	0.99359035944
$M = 36$	0.99597041165	0.99465068389	0.99359131823
$M = 39$	0.99597167542	0.99465179270	0.99359229578
$M = 42$	0.99597388048	0.99465276424	0.99359307411
$M = 45$	0.99597493628	0.99465336521	0.99359365248
$M = 48$	0.99597653285	0.99465338712	0.99359366322
$M = 51$	0.99597654286	0.99465339621	0.99359366271

In order to validate the correctness, a two-dimensional (2D) model with different electrodes is established in the coefficient-formed Partial Differential Equation (PDE) module of the COMSOL Multiphysics software. Taking the circular electrodes for example, its sketch map is shown in Figure 3.1. The center of the quartz plate, yellowed in Figure 3.1, contains the electrode which is surrounded by the annular gray unelectroded region. The outer area is set as the infinite element domain with its profile set as circular for simplicity, which is used to simulate the infinite boundary conditions. Here, the radius of the infinite element domain should be larger than twice of wavelength corresponding to the fundamental TSh mode considered here. The eigenvalue problem is solved, with the equation in PDE module expressed as

$$\lambda^2 e_a u - \lambda d_a \frac{\partial u}{\partial t} + \nabla \cdot \left(-c\nabla u - \alpha u + \gamma \right) + \beta \cdot \nabla u + au = f \tag{27}$$

where u represents the scalar displacement function to be solved and λ is the eigenvalue corresponding for the resonant frequency in this paper. Other coefficients such as e_a, d_a, c, α, β, γ, a and f are user-defined in which c is a coefficient matrix due to the material anisotropy. Matching with Eq. (27), the user-defined parameters in PDE module are listed as

$$e_a = 4\pi^2\rho, c = \begin{bmatrix} -M_n & 0 \\ 0 & -c_{55} \end{bmatrix}, a = -\rho\bar{\omega}_\infty^2, \alpha = d_a = \beta = \gamma = 0, \tag{28}$$

and

$$e_a = 4\pi^2\rho, c = \begin{bmatrix} -M_n & 0 \\ 0 & -c_{55} \end{bmatrix}, a = -\rho\omega_\infty^2, \alpha = d_a = \beta = \gamma = 0, \tag{29}$$

respectively for the electroded and unelectroded regions. Additionally, the continuous conditions between the electroded and unelectroded regions are satisfied automatically and Dirichlet boundary condition is set at the outmost circle boundary to simulate the radiation condition. Tables 3.3 shows the comparison between the theoretical results and those from FEM corresponding to the fundamental TSh modes in an infinite crystal plate covered by circular electrodes with different sizes. The theoretical resonant frequencies and modes shapes calculated via Eq. (30) coincide very well with those from the commercial software. Not limited by these, the cases of spurious TSh modes shown in Figure 3.2 and other electrodes shapes including rectangular, equilateral triangle, elliptical and regular pentagonal electrodes shown in Table 3.5 also shown the good consistency, which can efficiently validate the correctness of the theory proposed in this paper.
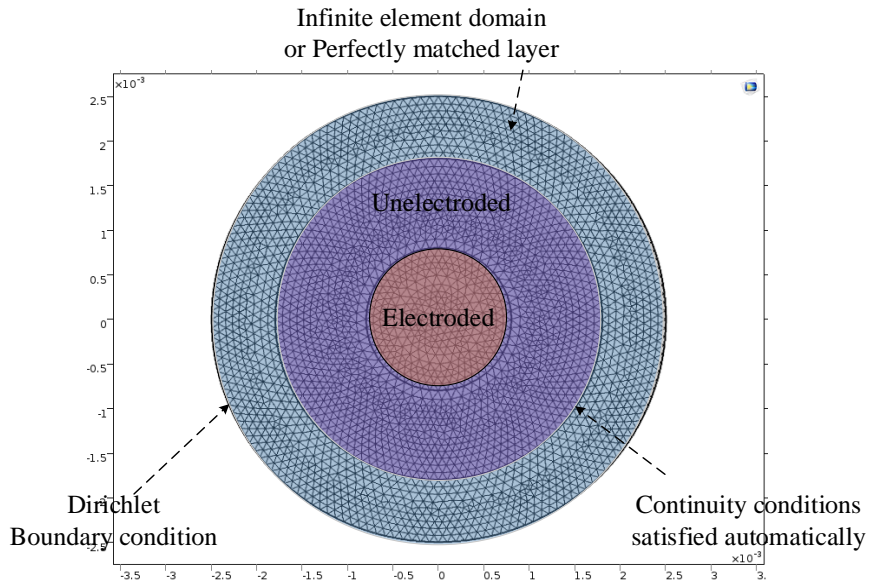
Figure 3.1   Schematic of FEM model

Table 3.3   The comparison between the theoretical and FEM results corresponding to the fundamental TSh mode for circular electrodes
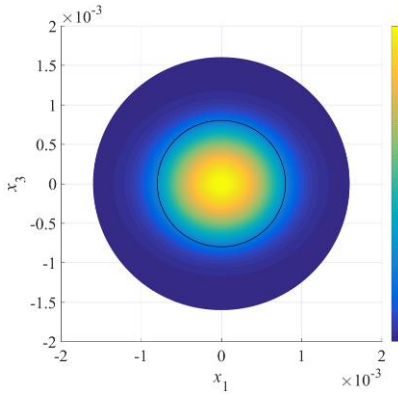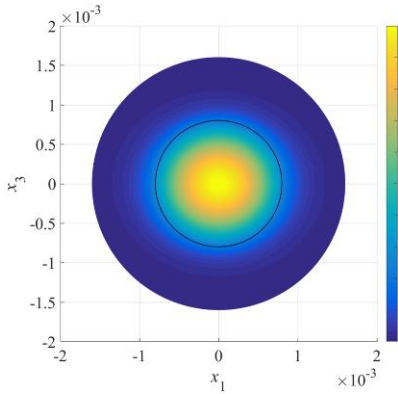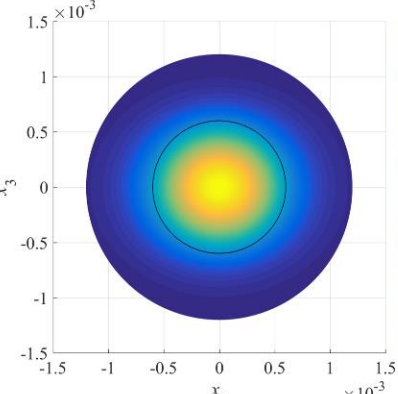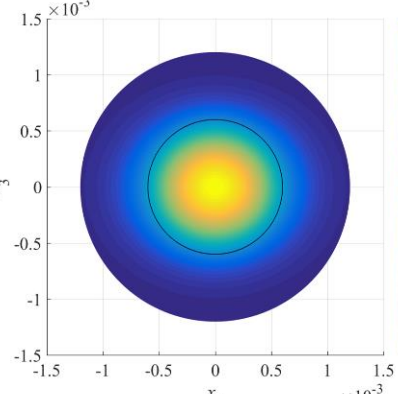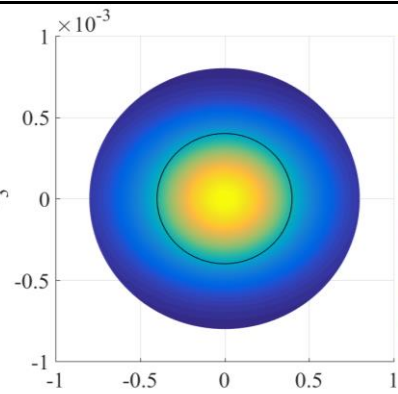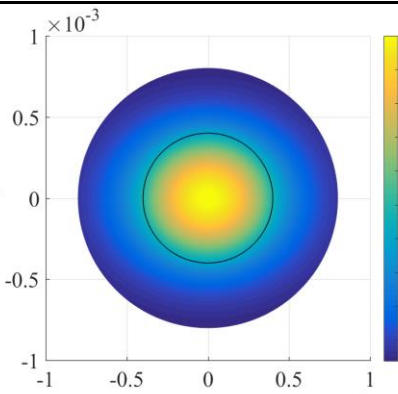
	Theoretical results proposed in this paper	FEM results from software
$2R_0$=1.6mm	f = 15.866317 MHz	f = 15.866316 MHz
$2R_0$=1.2mm	f = 15.957600 MHz	f = 15.957605 MHz
$2R_0$=0.8mm	f = 16.145162 MHz	f = 16.145167 MHz

Table 3.4   The comparison between the theoretical and FEM results corresponding to spurious
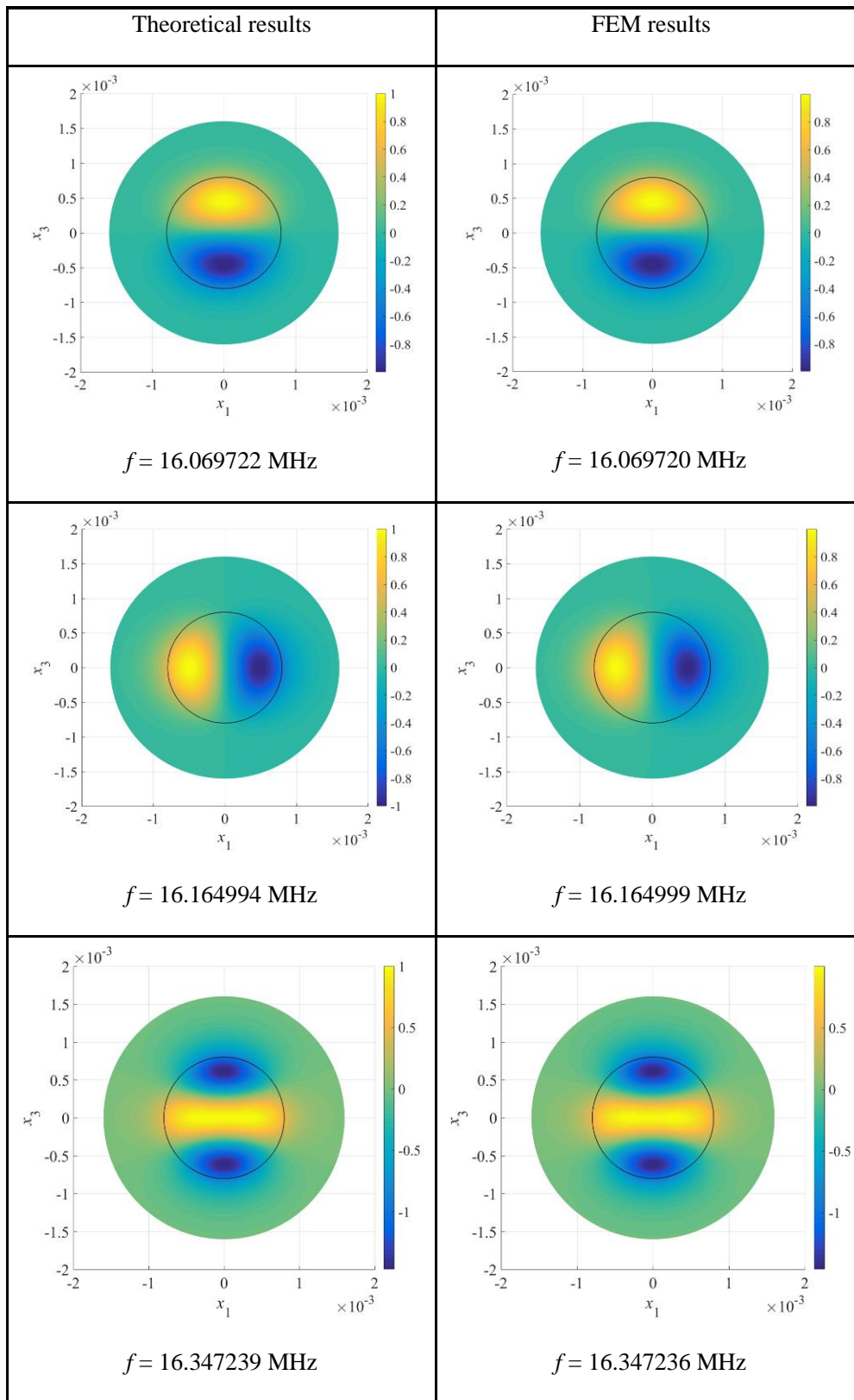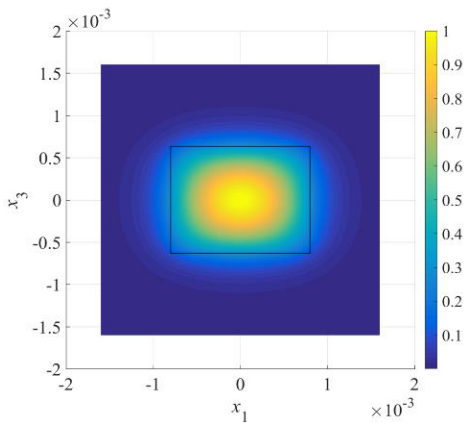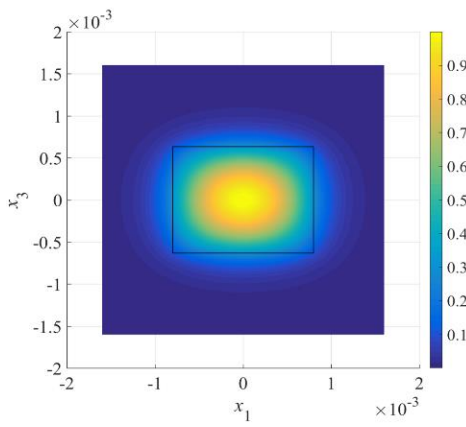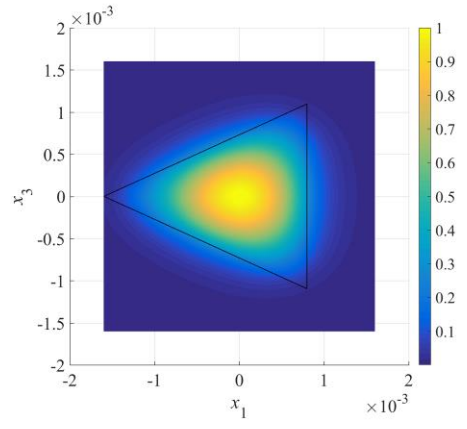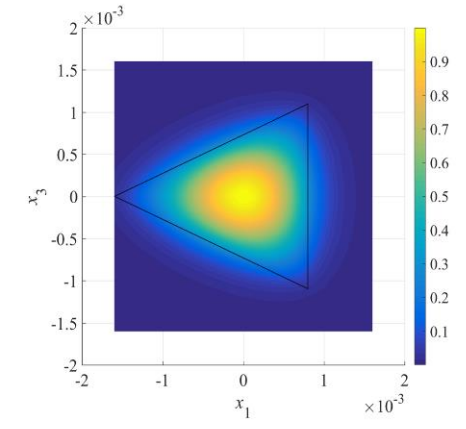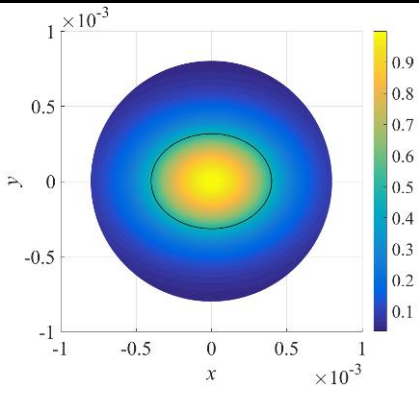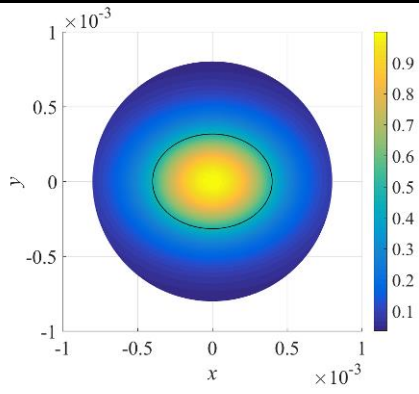
TSh modes for circular electrodes ($2R_0$ = 1.6 mm)

| Theoretical results	FEM results
$f = 16.069722$ MHz	$f = 16.069720$ MHz
$f = 16.164994$ MHz	$f = 16.164999$ MHz
$f = 16.347239$ MHz	$f = 16.347236$ MHz

Table 3.5　The comparisons between the theoretical and FEM results corresponding to the fundamental TSh mode for different electrode shapes

	Theoretical results	FEM results
Rectangular electrodes	$f = 15.869861$ MHz	$f = 15.869858$ MHz
Equilateral triangle electrodes	$f = 15.851460$ MHz	$f = 15.851459$ MHz
Elliptical electrodes	$f = 16.207542$ MHz	$f = 16.207540$ MHz

Regular pentagonal electrodes	$f = 15.807354$ MHz	$f = 15.807360$ MHz
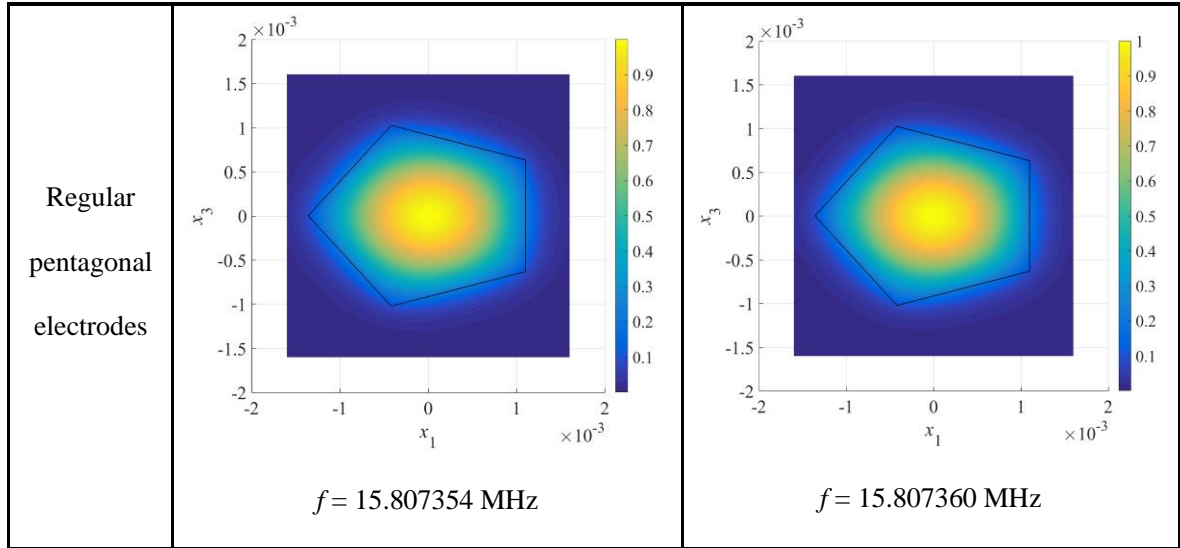
3.2. Analysis of irregularly-shaped electrodes

Reviewing Tables 3.3, 3.4, and 3.5, we can clearly see the energy trapping phenomenon, *i.e.*, the vibration mainly concentrates in the electroded region and exponentially decay in the unelectroded region. Such as Eq. (10), the intrinsic frequency of fundamental TSh mode in an infinite bare plate without electrodes is represented by ω_∞, and that is $\bar{\omega}_\infty$ if the plate is fully covered by electrodes. The final frequency ω is larger than $\bar{\omega}_\infty$, which makes the TSh waves travelling freely in the plate region with electrodes. However, because it smaller than ω_∞, the TSh wave will decay in the flat plate without electrodes. Finally, the energy trapping phenomenon appears. It is very important for the structural design and engineering applications of electrical devices. Because of that, some affiliated mountings can be installed far away from the electrodes, so that the mutual interference between the vibration and mountings can be eliminated efficiently. It is noted from Table 3.4 that the frequency of the second-order TSh mode in the x_1 direction is 16.164994 MHz, which is different from that in the x_3 direction, *i.e.*, 16.069722 MHz. The discrepancy is caused by the material anisotropy [14]. Actually, because of anisotropy, the displacement nephogram of fundamental mode is elliptic rather than circular, with semi-major and semi-minor axes lying in the x_1 and x_3 directions, respectively.

Theoretically, regular pentagonal electrodes are polygonal electrodes with any two sides not parallel to each other. To some extent, the resonant modes cannot interfere in the resonant cavity, which has excellent performance in suppressing lateral spurious modes. Therefore, regular

pentagonal electrodes are taking into account during the following analysis. When external electrodes are attached on the upper and bottom surfaces of the crystal plate, the resonant frequency will decrease because of the affiliated inertial effect, such as the variation patterns of resonat frequencies with the outer radius R_0 and mass ratio R shown in Figs. 4.1 and 4.2. As R_0 and R increases, the resonant frequency decreases, and some new trapped modes appear. Physically, the vibration mainly focuses on the region with external electrodes and decays exponentially outside, which is the energy-trapping phenomenon. ×××补充完图 4.1 和 4.2 之后还要补充一下进一步这两幅图的分析。第一，图 4.1 和图 4.2 新模态的频率都是从 $2h = 1\text{mm}$ 及 $R = 0.05$ 时板的共振频率 ω_∞；其次，两幅图频率的变化趋势不同，频率随厚度的变化量更大，说明电极厚度的影响比电极长度影响更显著。此外，对于厚度的影响，频率的改变量与厚度基本上呈准线性，这种变化可以为实验测量提供方便条件。××× ×××

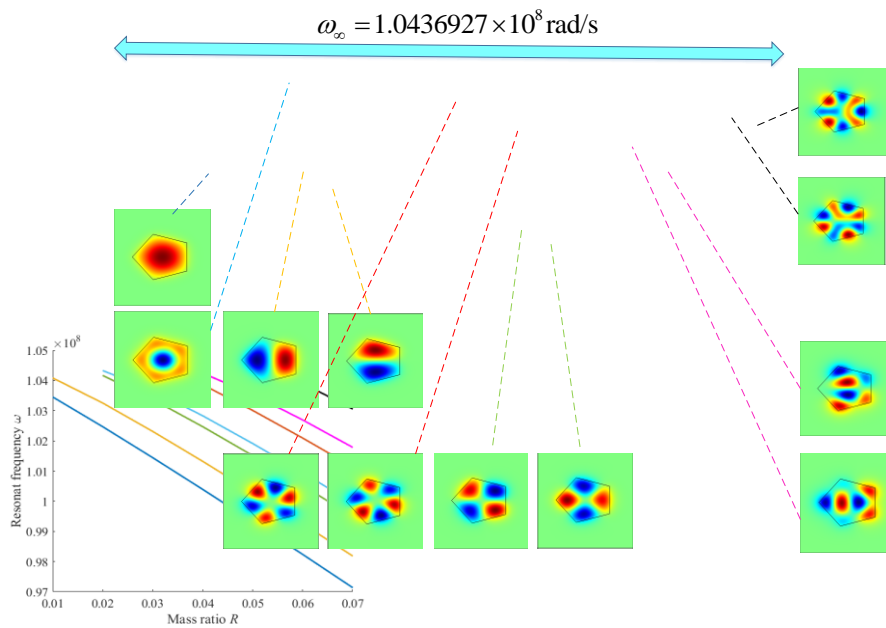$$\omega_\infty = 1.0436927 \times 10^8 \, \text{rad/s}$$

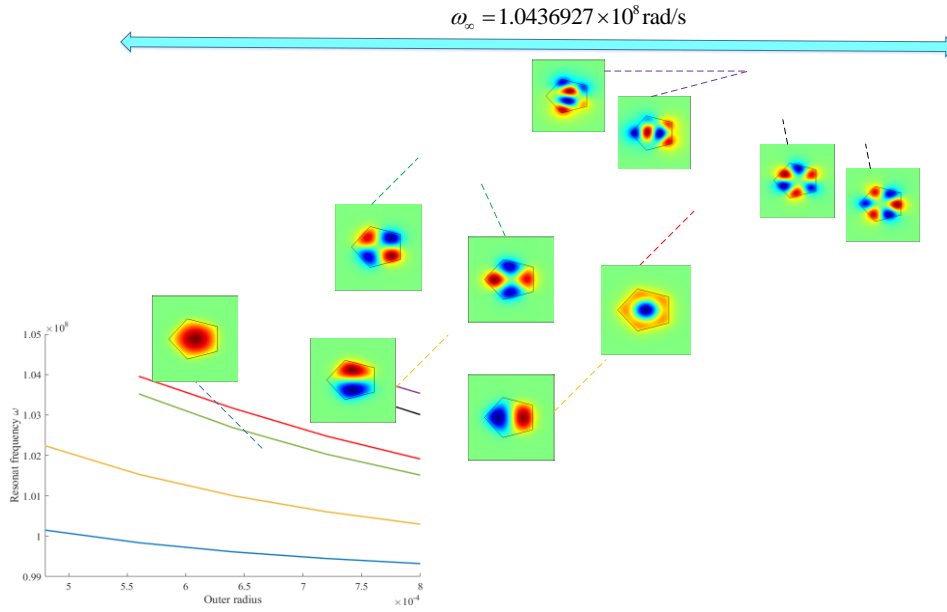Figure 4.1   Variation patterns of resonat frequencies with the mass ratio R

Figure 4.2　Variation patterns of resonat frequencies with the outer radius R_0 when $R = \times\times\times$

Generally speaking, higher-order modes, sometimes named as spurious modes have at least one nodal line inside the electroded region. The TSh strain changes its sign when encountering the nodal line, and then the corresponding charges produced through piezoelectricity will neutralize. As a consequence, the charge cancellation on the electrode may lead to a small output, which is undesirable during device applications. Therefore, we will concentrate the energy trapping of fundamental modes instead of the higher modes or unwanted spurious modes. For the fundamental mode, it is anticipated to produce a perfect "piston" mode with uniform displacement distribution in the active region. In this case, a uniform mass sensitivity distribution can be obtained, which is beneficial for sensing and detection. For qualitative analysis the pentagonal electrodes on the displacement distribution, Figs. 4.3 and 4.4 demonstrate effects of R_0 and R on the u_1 distribution along the x_1 and x_3 directions. For pentagonal electrodes with constant thickness, the electrode size in the x_1 and x_3 direction determine the displacement distribution, such as Fig. 4.3. Smaller electrodes will lead to more concentrated vibration near the center. Therefore, for obtaining an ideally flat displacement distribution in the center of electrodes, the outer radius R_0 should be relatively larger. By contrast, for a fixed lateral size R_0, the thickness has negligible effect on u_1, such as Fig. 4.4. It is understandable because the vibration mainly focuses on the electrode region.

When the thickness increases homogeneously, the electrode distribution in the x_1-x_3 plane is not changed, which determines the u_1 distribution in Fig. 4.4
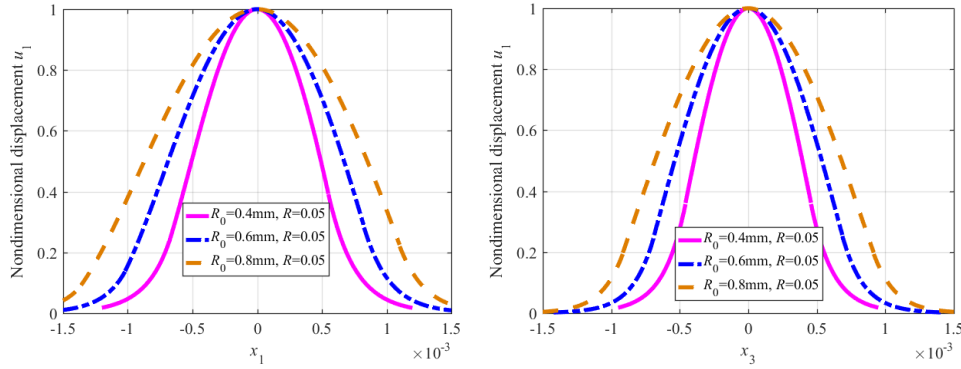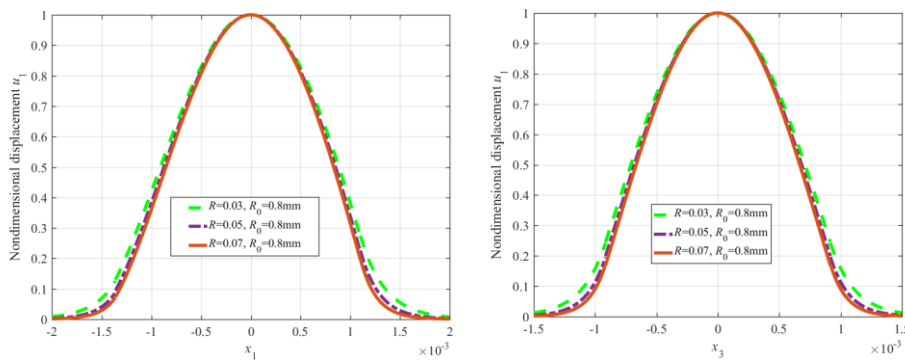

Figure 4.3   Effect of the radius R_0 on the distribution of u_1 along (a) x_1 and (b) x_3 directions, in which the resonant frequency is ×××MHz, ×××MHz and ×××MHz when R_0 is 0.4mm, 0.6mm and 0.8mm, respectively).

Figure 4.4   Effect of the mass ratio R on the distribution of u_1 along x_1 (a) and x_3 directions, in which the resonant frequency is 16.144872MHz, 15.807354MHz and 15.459200MHz when R is 0.03, 0.05 and 0.07, respectively).

4. Conclusion

In this paper, a novel analytical approach is presented to analyze the TSh vibration of partially-electroded AT-cut quartz resonators with irregularly-shaped electrodes. Five kinds of electrodes with different profiles, *i.e.*, circle, ellipse, equilateral triangle, rectangle and regular pentagon, are included. ×××× This method exhibits good convergence and high accuracy after

numerically verified via FEM simulations. Based on this method, the working performance of this quartz crystal plate with pentagonal electrodes, including resonant frequency and mode shape, are investigated in detail, and the effects of electrode size and mass ratio are analyzed. The method proposed and results obtained provide theoretical guides for the structural design and manufacturing of resonators in engineering applications. ××××

Acknowledgements

References

[1] Plausinaitis D, Sinkevicius L, Samukaite-Bubniene U, et al. Evaluation of Electrochemical Quartz Crystal Microbalance Based Sensor Modified by Uric Acid-imprinted Polypyrrole. Talanta, 2020: 121414.

[2] Rianjanu A, Julian T, Hidayat S N, et al. Quartz crystal microbalance humidity sensors integrated with hydrophilic polyethyleneimine-grafted polyacrylonitrile nanofibers[J]. Sensors and Actuators B Chemical, 2020, 319:128286.

[3] Tiersten, H.F., Thickness vibrations of piezoelectric plates. Journal of the Acoustical Society

of America. 1963, 35, 53–58.

[4] Tiersten, H.F., A corrected modal representation of thickness vibrations in quartz plates and its influence on the transversely varying case. IEEE Transactions on Ultrasonics, Ferroelectrics, and Frequency Control, 2003, 50: 1436-1443.

[5] Tiersten, H.F., Analysis of trapped-energy resonators operating in overtones of coupled thickness shear and thickness twist. Journal of the Acoustical Society of America, 1976, 59(4), pp. 879–888.

[6] Hartz, Jequil S. R., et al. Investigation of Energy Trapping of the Lateral Field Excited Thickness Shear Mode in AT-Cut Quartz Crystal Microbalances. IEEE International Ultrasonics Symposium, 2019: 596-599.

[7] Zhu F, Li P, Dai X, Qian Z, Kuznetsova IE, Kolesov V, et al. A Theoretical Model for Analyzing the Thickness-Shear Vibration of a Circular Quartz Crystal Plate With Multiple Concentric Ring Electrodes. IEEE transactions on ultrasonics, ferroelectrics, and frequency control. 2021; 68(5): 1808-18.

[8] Li Yu, et al. A homotopy shape solution for thickness-vibration of centrally partially electrode regular polygonal AT-cut quartz resonators, 13th Symposium on Piezoelectrcity, Acoustic Waves, and Device Applications (SPAWDA). 2019.

[9] Wang, W., Wu, R., Wang, J., Du, J., & Yang, J.. Thickness-shear modes of an elliptical, contoured at-cut quartz resonator. IEEE Transactions on Ultrasonics, Ferroelectrics, and Frequency Control, 60(6), 1192–1198. 2013

[10] Tiersten, H.F., On the accurate description of piezoelectric resonators subject to biasing deformations. International Journal of Engineering Science, 1995, 33(15), pp. 2239–2259.

[11] Shi Junjie, Fan Cuiying, Zhao Minghao. Effects of Electrode Off Centre on Trapped Thickness-Shear Modes in Contoured AT-Cut Quartz Resonators. International Journal of Acoustics and Vibration, vol. 23, no. 4, pp. 423-431, 2018.

[12] Wu RX, et al. Effects of Elliptical Ring Electrodes on Shear Vibrations of Quartz Crystal Plates. International Journal of Acoustics and Vibration, vol. 24, no. 3, pp. 586-591, 2019.

[13] H. J. He, J. X. Liu and J. S. Yang, Thickness-shear and thickness-twist vibrations of an AT-cut quartz mesa resonator. IEEE Transactions on Ultrasonics, Ferroelectrics and Frequency

Control, vol. 58, no. 10, pp. 2050-2055, 2011.

[14] H. J. He, J. S. Yang, J. A. Kosinski, Shear-horizontal vibration modes of an oblate elliptical cylinder and energy trapping in contoured acoustic wave resonators, IEEE Transactions on Ultrasonics, Ferroelectrics and Frequency Control, vol. 59, no. 8, pp. 1774-1780, 2012.

[15] Steward J.T., Yong Y.K. Thickness-shear mode shapes and mass-frequency influence surface of a circular and electroded AT-cut quartz resonator. IEEE Transactions on Ultrasonics, Ferroelectrics and Frequency Control, 1992, 39, 609–617.

[16] Liu B., Xing Y.F., Thickness-shear vibration analysis of rectangular quartz plates by a differential quadrature finite element method. AIP Conf. Proc. 2014, 41, 41–44.

[17] Liu, B.; Xing, Y.F.; Wang, W.; Yu, W.D. Thickness-shear vibration analysis of circular quartz crystal plates by a differential quadrature hierarchical finite element method. Compos. Struct. 2015, 131, 1073–1080.

[18] Mindlin, R.D., High frequency vibrations of crystal plates. Quarterly of Applied Mathematics, 1961, 19(1): 51-61.

[19] Tiersten, H.F. and Mindlin, R.D., Forced vibrations of piezoelectric crystal plates. Quarterly of Applied Mathematics, 1962, 20(2): 107-119.

[20] Mindlin, R.D. An Introduction to the Mathematical Theory of Vibrations of Elastic Plates; Yang, J., Ed.; World Scientific: Singapore, December 2006.

[21] Wang, J. and Yang J.S., High-order theories of piezoelectric plates and applications. Applied Mechanics Reviews, 2000, 53(4): 87-99.

[22] Tiersten H.F., Smythe R.C., Coupled thickness-shear and thickness-twist vibrations of unelectroded AT-cut quartz plates. Journal of the Acoustical Society of America, 1985, 78, 1684–1689.

[23] Zhou, Y.S., Tiersten, H.F.. On the normal acceleration sensitivity of contoured quartz resonators stiffened by quartz cover plates supported by clips. Journal of Applied Physics, 1992, 72(4), pp. 1244–1254.

[24] Tiersten H.F., Smythe R.C. An analysis of contoured crystal resonators operating in overtones of coupled thickness shear and thickness twist. Journal of the Acoustical Society of America, 1979, 65, 1455–1460.

[25] He H.J., Liu J.X., Yang, J.S. Effects of mismatched electrodes on an AT-cut quartz resonator. IEEE Transactions on Ultrasonics, Ferroelectrics and Frequency Control, 2012, 59, 281–286.

[26] Feng Zhu, Bin Wang, Xiaoyun Dai, Zhenghua Qian, Iren Kuznetsova, Vladimir Kolesov, and Bin Huang, Vibration optimization of an infinite circular AT-cut quartz resonator with ring electrodes, Applied Mathematical Modelling, Vol. 72, pp. 217-229, August, 2019.

[27] Tiersten, H.F., Sinha, B.K., Temperature dependence of the resonant frequency of electroded doubly-rotated quartz thickness-mode resonators, Journal of Applied Physics, 1979, 50(12), pp. 8038–8051.

[28] H. He, J. Yang, J. A. Kosinski and H. Zhang, Scalar Differential Equations for Transversely Varying Thickness Modes in Doubly Rotated Quartz Crystal Sensors, in IEEE Sensors Letters, vol. 2, no. 3, pp. 1-4, Sept. 2018.

[29] Tiersten, H.F., On the accurate description of piezoelectric resonators subject to biasing deformations, International Journal of Engineering Science, 1995, 33(15), pp. 2239–2259.

[30] Tiersten, H.F., Sinha, B.K., Temperature dependence of the resonant frequency of electroded doubly-rotated quartz thickness-mode resonators Journal of Applied Physics, 1979, 50(12), pp. 8038–8051.

[31] Feng Zhu, Bin Wang, Zhenghua Qian, and Ernian Pan, Accurate characterization of 3D dispersion curves and mode shapes of waves propagating in generally anisotropic viscoelastic/elastic plates, International Journal of Solids and Structures, Vol. 150, pp. 52-65, October, 2018.